

Expansion series of the pairwise velocity generating function and its implications on redshift space distortion modeling

Junde Chen¹, Pengjie Zhang^{1,2,3} and Yi Zheng⁴

¹ Department of Astronomy, Shanghai Jiao Tong University, Shanghai 200240, China
jundechen@sjtu.edu.cn

² Shanghai Key Laboratory for Particle Physics and Cosmology, People's Republic of China

³ Tsung-Dao Lee Institute, Shanghai 200240, People's Republic of China

⁴ School of Physics and Astronomy, Sun Yat-sen University, 2 Daxue Road, Tangjia, Zhuhai, 519082, People's Republic of China Received 20xx month day; accepted 20xx month day

Abstract The pairwise velocity generating function G has deep connection with both the pairwise velocity probability distribution function and modeling of redshift space distortion (RSD). Its implementation into RSD modeling is often facilitated by expansion into series of pairwise velocity moments $\langle v_{12}^n \rangle$. Motivated by the logarithmic transformation of the cosmic density field, we investigate an alternative expansion into series of pairwise velocity cumulants $\langle v_{12}^n \rangle_c$. We numerically evaluate the convergence rate of the two expansions, with three 3072³ particle simulations of the CosmicGrowth N-body simulation series. (1) We find that the cumulant expansion performs significantly better, for all the halo samples and redshifts investigated. (2) For modeling RSD at $k_{\parallel} < 0.1h \text{ Mpc}^{-1}$, including only the $n = 1, 2$ cumulants is sufficient. (3) But for modeling RSD at $k_{\parallel} = 0.2h \text{ Mpc}^{-1}$, we need and only need the $n = 1, 2, 3, 4$ cumulants. These results provide specific requirements on RSD modeling in terms of m -th order statistics of the large scale structure.

Key words: cosmology: dark energy, dark matter, large-scale structure of universe

1 INTRODUCTION

One of the most important issues in cosmology is to interpret the cosmic acceleration (Riess et al. 1998; Perlmutter et al. 1999). Both dark energy and modified gravitational theories can produce the same expansion history. Yet, they predict the different growth histories of the structure. Therefore, in observation, one can distinguish them by testing the structure growth rate $f(z)\sigma_8(z)$ through redshift-space distortion (RSD) (Peebles 1980; Kaiser 1987; Scoccimarro 2004). The observed position of galaxy in redshift space will be distorted by its peculiar velocity along the line of sight due to the Doppler shift. This RSD effect turns the isotropic distributed pattern of galaxies in real space into the anisotropic one in redshift space. Since peculiar velocity directly reflects the structure growth, by modeling the mapping from real space to redshift space, the peculiar velocity information can be extracted and used to constrain the cosmology.

Over the past decades, RSD has been proved to be a very powerful cosmological probe and adopted in many observational projects, such as 2dFGS (Peacock et al. 2001; Hawkins et al. 2003), SDSS (Tegmark et al. 2006; Reid et al. 2012; Samushia et al. 2012; Tojeiro et al. 2012; Chuang et al. 2013), VVDS (Guzzo et al. 2008), WiggleZ (Blake et al. 2011), 6dFGS (Beutler et al. 2012; Johnson et al. 2014), GAMA (Simpson et al. 2016), VIPERS (de la Torre et al. 2013; Pezzotta et al. 2017;

Mohammad et al. 2018), FastSound (Okumura et al. 2016), BOSS (White et al. 2015; Howlett et al. 2015; Li et al. 2016; Alam et al. 2017) and eBOSS (Tamone et al. 2020; Bautista et al. 2020). In near future, the ongoing and upcoming dark energy surveys like DESI, PFS, Euclid, SKA, WFIRST (e.g. DESI Collaboration et al. (2016); Amendola et al. (2018); Abdalla et al. (2015); Spergel et al. (2015)) will have the ability to constrain the structure growth rate at $\sim 1\%$ or even higher accuracy level. However, this target precision presents a sever challenge to the RSD modeling.

The difficulties of accurate RSD modeling come from three key ingredients. (1) One is the mapping between real space and redshift space (Peebles 1980; Scoccimarro 2004). The mapping is nonlinear. For example, the redshift space 2-pt correlation function is determined by not only the two-point correlation function in real space, but all the n -th order correlation functions. It is also nonlocal, that real space clustering at real scales can have significant contribution to a given scale in redshift space. (2) One is the nonlinear evolution of the matter/halo density and velocity field, a long standing challenge in modern cosmology. (3) The third is the nonlinear (and nonlocal) galaxy-halo-matter relation in not only the position space, but the whole phase space (Desjacques et al. 2018a; Huterer & Shafer 2018; Chen et al. 2018; Zhang 2018). RSD models usually treat the redshift space correlation function or power spectrum as a expansion to a series of the density and velocity field statistics in real space. For example, the distribution function approach (Seljak & McDonald 2011) expresses the redshift space density in terms of series of summation of velocity moments, then obtain the redshift space power spectrum from the correlators between the Fourier components of these moments. Okumura et al. (2012a,b) investigate the contribution of each correlator in N-body simulations and give a conclusion that the accurate measurement of the redshift space power spectrum to $k \simeq 0.2h \text{ Mpc}^{-1}$ at $z = 0$ and $k \simeq 0.3h \text{ Mpc}^{-1}$ at $z = 2$ require 6th order moment statistics to be taken into account. The Fourier streaming model (Vlah & White 2019) expand the redshift space power spectrum with cumulant theorem. Chen et al. (2020) compare the moment expansion approach and the Fourier streaming model in N-body simulation halo samples. They conclude that the expansions have good agreement with the power spectrum at the percent level when third order velocity statistics is taken into account except those close to line of sight direction, while the forth order will break this agreement for $k > 0.2h \text{ Mpc}^{-1}$. Generally, existing models treat the large-scale velocity with perturbation theory then add the small scale Finger-of-God effect induced by the random motion in small scale, or assume a certain type of velocity distribution. These approaches will mix all the non-linear effects together and make it difficult to quantify the influence of each individually.

In this paper, we take a step back from these works and restrict our study to the first ingredient. The question that we aim to ask is that, to accurately describe the real space-redshift space mapping, what LSS statistics must be included. As known in the literature (Scoccimarro 2004), the mapping is fully determined by the pairwise velocity generating function G , this question then reduces to (1) what expansion shall we adopt to describe G , and (2) which order of pairwise velocity moments shall we include in the expansion.

In our previous work (Zhao & Chen 2021), we directly evaluated the generating function G at redshift $z = 0$ in dark matter field. We also proposed a new RSD statistics $P^s(k_{\parallel}, r_{\perp})$ which is more convenient to evaluate in the context of G . In this work, we present the more comprehensive investigations to generating function, including the halo mass and redshift dependence. We push the redshift to $z = 1.5$ which is close to the interest of DESI, PFS, Euclid and SKA. And most importantly, we quantify the contribution from individual moments to G and evaluate its impact to the hybrid statistics $P^s(k_{\parallel}, r_{\perp})$. Furthermore, we also investigate the influence of Gaussian and exponential as the pairwise velocity PDF to the measurement of generating function G . Zhang et al. (2013) provides a method to decompose the peculiar velocity in different components with different features, which can help us to better understanding the peculiar velocity field and RSD modeling. We also use the similar method in this work, to investigate the contributions and behaviors of G for the different components.

We organize this paper as follows. In Section2, we provide a brief review of RSD modeling and its relation with the pairwise velocity moment generating function. Then we derive two independent approaches to measure the moment generating function in simulation. Section3 introduces the simulation

and halo catalogs we adopt for numerical evaluation of the related quantities. The main results are presented in Section 4. Finally, Section 5 summarizes our major findings.

2 PAIRWISE VELOCITY GENERATING FUNCTION AND RSD MODELING

Comoving peculiar velocity \mathbf{v} of a galaxy adds a Doppler redshift on top of the cosmological redshift, $z^{\text{obs}} = z + v_{\parallel}/c$. Here $v_{\parallel} = \mathbf{v} \cdot \hat{x}$ is the velocity component along the line of sight \hat{x} . Therefore the observed position \mathbf{s} of the galaxy in the redshift space is changed with respect to its real space position \mathbf{x} ,

$$\mathbf{s} = \mathbf{x} + \frac{\mathbf{v} \cdot \hat{x}}{H(z)} \hat{x} = \mathbf{x} + \frac{v_{\parallel}}{H(z)} \hat{x}. \quad (1)$$

Here $H(z)$ is the Hubble parameter at redshift z . For brevity we will neglect H in the denominator, so \mathbf{v} hereafter should be interpreted as \mathbf{v}/H . The redshift space galaxy number density is then,

$$n^s(\mathbf{s}) = \bar{n}(1 + \delta^s(\mathbf{s})) = \sum_{\alpha} \delta_{3D}(\mathbf{s} - [\mathbf{x}_{\alpha} + v_{\parallel, \alpha} \hat{x}_{\alpha}]). \quad (2)$$

The sum is over all galaxies ($\alpha = 1, 2, \dots$) considered. The Fourier transform of the overdensity δ^s is then

$$\bar{n} [\delta^s(\mathbf{k}) + (2\pi)^3 \delta_{3D}(\mathbf{k})] = \sum_{\alpha} \exp(i\mathbf{k} \cdot [\mathbf{x}_{\alpha} + v_{\parallel, \alpha} \hat{x}_{\alpha}]). \quad (3)$$

2.1 Power spectrum based models

The redshift space power spectrum $P^s(\mathbf{k})$ is defined through

$$\langle \delta^s(\mathbf{k}) \delta^s(\mathbf{k}') \rangle = (2\pi)^3 \delta_{3D}(\mathbf{k} + \mathbf{k}') P^s(\mathbf{k}). \quad (4)$$

We then obtain

$$\bar{n}^2 V (P^s(\mathbf{k}) + (2\pi)^3 \delta_{3D}(\mathbf{k})) = \left\langle \sum_{\alpha\beta} e^{ik_{\parallel} v_{\alpha\beta}} e^{i\mathbf{k} \cdot \mathbf{r}'_{\alpha\beta}} \right\rangle. \quad (5)$$

Here we have adopted a fixed line of sight. $v_{\alpha\beta} \equiv v_{\parallel, \alpha} - v_{\parallel, \beta}$, $\mathbf{r}' \equiv \mathbf{x}_{\alpha} - \mathbf{x}_{\beta}$. In the continuum limit, the above result reduces to the more familiar form,

$$P^s(\mathbf{k}) = \int \left(\langle (1 + \delta_1)(1 + \delta_2) e^{ik_{\parallel} v_{12}} \rangle_{\mathbf{r}'} - 1 \right) e^{i\mathbf{k} \cdot \mathbf{r}'} d^3 \mathbf{r}'. \quad (6)$$

in which $\delta_i \equiv \delta(\mathbf{x}_i)$ ($i = 1, 2$), $\mathbf{r}' \equiv \mathbf{x}_1 - \mathbf{x}_2$, $v_{12} \equiv v_{\parallel}(\mathbf{x}_1) - v_{\parallel}(\mathbf{x}_2)$. $\langle \dots \rangle$ denotes the ensemble average. The subscript means the ensemble average is taken at a fixed pair separation \mathbf{r}' .

The above results are widely known in the literature (e.g. Scoccimarro (2004)). Several models of RSD are based upon Eq. 6, or Eq. 5 or its equivalent forms (e.g. Scoccimarro (2004); Matsubara (2008); Taruya et al. (2010); Seljak & McDonald (2011); Okumura et al. (2012a); Zhang et al. (2013); Zheng et al. (2013); Zheng & Song (2016); Song et al. (2018); Zheng et al. (2019)).

2.2 Correlation function based models

The redshift space correlation function is also modelled with the streaming model (Peebles 1980),

$$1 + \xi^s(\mathbf{r} = (r_{\parallel}, \mathbf{r}_{\perp})) = \int \left(1 + \xi(\mathbf{r}' = (r'_{\parallel}, \mathbf{r}_{\perp}))\right) p(v_{12} | \mathbf{r}' = (r'_{\parallel}, \mathbf{r}_{\perp})) dr'_{\parallel}, \quad (7)$$

where \mathbf{r}_{\perp} is the component of the separation in the perpendicular direction to the line of sight. $p(v_{12}|\mathbf{r})$ is the pairwise velocity PDF at separation \mathbf{r} .

Eq.7 is exact. Nevertheless, $p(v_{12})$ is poorly understood in theory and approximations of it are inevitable in practice. The Gaussian streaming model (Reid & White 2011) takes the assumption $p(v_{12})$ distributes as the Gaussian function with a non zero mean $\langle v_{12} \rangle$ and dispersion σ_{12} . A further problem is that, it is difficult to find a suitable parametric form for $p(v_{12})$ (Fisher 1995; Sheth 1996; Juszkiewicz et al. 1998; Scoccimarro 2004; Tinker 2007; Bianchi et al. 2015, 2016; Kuruvilla & Porciani 2018; Cuesta-Lazaro et al. 2020).

2.3 Pairwise velocity generating function and RSD modeling

The above two statistics can be unified by the pairwise velocity generating function (Scoccimarro 2004),

$$G(k_{\parallel}, \mathbf{r}) = \frac{\langle (1 + \delta_1)(1 + \delta_2)e^{ik_{\parallel}v_{12}} \rangle}{1 + \xi(r)}, \quad (8)$$

where $\xi(r) = \langle \delta_1 \delta_2 \rangle$ is the two point correlation function in real space. One can verify that G is the generating function of the pairwise velocity,

$$\langle v_{12}^m \rangle \equiv \frac{\langle (1 + \delta_1)(1 + \delta_2)v_{12}^m \rangle}{1 + \xi(r)} = \left. \frac{\partial^m G}{\partial (ik_{\parallel})^m} \right|_{k_{\parallel}=0}, m \geq 1. \quad (9)$$

For the discrete distribution, the generating function should be defined by and evaluated through

$$G(k_{\parallel}, \mathbf{r}) \equiv \frac{\langle \sum_{\alpha\beta} \exp(ik_{\parallel}v_{\alpha\beta}) \rangle_{\mathbf{r}_{\alpha\beta}=\mathbf{r}}}{\langle \sum_{\alpha\beta} \rangle_{\mathbf{r}_{\alpha\beta}=\mathbf{r}}}. \quad (10)$$

Here the ensemble average is over pairs with separation $\mathbf{r}_{\alpha\beta} = \mathbf{r}$. When $r \rightarrow \infty$ that we can neglect spatial correlations in the density and velocity fields,

$$G(k_{\parallel}, r \rightarrow \infty) \equiv G_{\infty} = \langle e^{ik_{\parallel}v_{\alpha}} \rangle^2. \quad (11)$$

This quantity is positive, and describes the Finger of God effect (e.g. Zhang et al. (2013); Zheng et al. (2013)).

The pairwise velocity generating function plays an important role in RSD modelling.

- First, it determines the redshift power spectrum in Fourier space,

$$P^s(\mathbf{k}) = \int \left[\left(1 + \xi(r')\right) G(k_{\parallel}, \mathbf{r}') - 1 \right] e^{i\mathbf{k}\cdot\mathbf{r}'} d^3 \mathbf{r}'. \quad (12)$$

- Second, it determines the pairwise velocity PDF and therefore the RSD modelling in configuration space.

$$p(v_{12} | \mathbf{r}) = \int G(k_{\parallel}, \mathbf{r}) e^{ik_{\parallel}v_{12}} \frac{dk_{\parallel}}{2\pi}. \quad (13)$$

- The above relations are well known in the literature (e.g. [Scoccimarro \(2004\)](#); [Taruya et al. \(2010\)](#); [Desjacques et al. \(2018b\)](#)), but have not fully incorporated in RSD modelling. Furthermore, we can define a hybrid statistics $P^s(k_{\parallel}, r_{\perp})$. By multiplying both sides of Eq.12 by $\int \exp(-i\mathbf{k}_{\perp} \cdot \mathbf{r}_{\perp}) d^2\mathbf{k}_{\perp}/(2\pi)^2$, we obtain

$$P^s(k_{\parallel}, r_{\perp}) = \int [(1 + \xi(r)) G(k_{\parallel}, \mathbf{r}) - 1] e^{ik_{\parallel} r_{\parallel}} dr_{\parallel}. \quad (14)$$

This is neither the correlation function nor the power spectrum. But this hybrid statistics has some attractive features. (1) Since $G(k_{\parallel} = 0) = 1$, $P^s(k_{\parallel} = 0, r_{\perp}) = \int_{-\infty}^{\infty} \xi(r_{\parallel}, r_{\perp}) dr_{\parallel} = w_p(r_{\perp})$. Namely, the $k_{\parallel} = 0$ mode equals the projected correlation function w_p ,¹ therefore, it is unaffected by RSD, which is only constrained to $k_{\parallel} \neq 0$ modes. This is an advantage that $P^s(\mathbf{k})$ also share. But ξ^s does not have this advantage, since $\xi^s(r_{\parallel}, r_{\perp})$ of all configurations are affected by RSD. (2) Within the context of RSD modelling with the generating function G , this is the most straightforward to numerically implement, since only one integral over r_{\parallel} is needed. (3) In the measurement, it is also straightforward to convert from the measurement of correlation function, which has better handling over survey masks and varying line of sight.

2.4 Moment and cumulant expansion of the generating function

One intrinsic advantage is that G can be naturally Taylor expanded with physically meaningful Taylor coefficients. This can be implemented either with the moment expansion or with the cumulant expansion.

2.4.1 Moment expansion

The moment expansion directly expands G into its Taylor expansion series,

$$\begin{aligned} G(k_{\parallel}, \mathbf{r}) &= 1 - \sum_{m \geq 1} (-1)^{m-1} \frac{\langle v_{12}^{2m} \rangle}{(2m)!} k_{\parallel}^{2m} + i \sum_{m \geq 1} (-1)^{m-1} \frac{\langle v_{12}^{2m-1} \rangle}{(2m-1)!} k_{\parallel}^{2m-1} \\ &= 1 + i \langle v_{12} \rangle k_{\parallel} - \frac{1}{2} \langle v_{12}^2 \rangle k_{\parallel}^2 - \frac{1}{6} i \langle v_{12}^3 \rangle k_{\parallel}^3 + \frac{1}{24} \langle v_{12}^4 \rangle k_{\parallel}^4 + \dots \end{aligned} \quad (15)$$

The convergence rate of Eq.15 is decided by the coefficients of pairwise velocity moments. Through numerical simulations, we can robustly quantify the impact of individual terms and determine the moments which must be included to reach the desired accuracy in RSD.

2.4.2 Cumulant expansion

Eq. 15 is not the only way of expanding G in velocity moments. Instead we can Taylor expand $\ln G$ in power series of k_{\parallel} . The expansion coefficients turn out to be the pairwise velocity cumulants $\langle v_{12}^m \rangle_c$. [Scoccimarro \(2004\)](#) already pointed out $\ln G$ as the cumulant generating function, but did not specify the cumulant expansion coefficient as $\langle v_{12}^m \rangle_c$. Therefore we provide a proof here. Furthermore, we find that such relation is connected to the widely adopted logarithmic transformation of the cosmic density field.

Defining an auxiliary field

$$y \equiv \ln(1 + \delta) - \langle \ln(1 + \delta) \rangle, \quad (16)$$

¹ The projected correlation function $w_p(r_{\perp})$ is often redefined as $w_p(r_{\perp})/r_{\perp}$ to make it dimensionless.

and setting $\lambda = ik_{\parallel}$, we have

$$\begin{aligned}
G(\lambda | \mathbf{r}) &\equiv \frac{\langle (1 + \delta_1)(1 + \delta_2) \exp(\lambda v_{12}) \rangle}{\langle (1 + \delta_1)(1 + \delta_2) \rangle} \\
&= \frac{\langle \exp[(y_1 + y_2) + \lambda v_{12}] \rangle}{\langle (1 + \delta_1)(1 + \delta_2) \rangle} \\
&= \frac{1}{1 + \xi(r)} \exp \left[\sum_{n \geq 2} \frac{\langle ((y_1 + y_2) + \lambda v_{12})^n \rangle_c}{n!} \right] \\
&= \exp \left[\sum_{m \geq 1} \frac{c_m(\mathbf{r})}{m!} \lambda^m \right]. \tag{17}
\end{aligned}$$

Here,

$$c_m \equiv m! \sum_{n \geq 2, n \geq m} \frac{C_{n-m}^{n-m} \langle (y_1 + y_2)^{n-m} v_{12}^m \rangle_c}{n! (1 + \xi(r))}. \tag{18}$$

Furthermore, we find

$$c_1 = \langle v_{12} \rangle \equiv \langle v_{12} \rangle_c, \tag{19}$$

$$c_2 = \langle (v_{12} - c_1)^2 \rangle \equiv \langle v_{12}^2 \rangle_c \tag{20}$$

$$c_3 = \langle (v_{12} - c_1)^3 \rangle \equiv \langle v_{12}^3 \rangle_c \tag{21}$$

$$c_4 = \langle (v_{12} - c_1)^4 \rangle - 3 \langle (v_{12} - c_1)^2 \rangle^2 \equiv \langle v_{12}^4 \rangle_c, \dots \tag{22}$$

Namely the cumulant expansion coefficient c_m is the pairwise velocity cumulant $\langle v_{12}^m \rangle_c$. Then we obtain the cumulant expansion of pairwise velocity generating function,

$$\ln G(k_{\parallel}, \mathbf{r}) = - \sum_{m \geq 1} (-1)^{m-1} \frac{\langle v_{12}^{2m} \rangle_c}{(2m)!} k_{\parallel}^{2m} + i \sum_{m \geq 1} (-1)^{m-1} \frac{\langle v_{12}^{2m-1} \rangle_c}{(2m-1)!} k_{\parallel}^{2m-1}. \tag{23}$$

Namely $\ln G$ is the cumulant generating function of pairwise velocity, versus G as the moment generating function of pairwise velocity. We may have expected this correspondence from the moment/cumulant generating function of the density field.

We may expect that the above expansion converges faster than the expansion with Eq. 15. The reason is that the density field is close to lognormal and the velocity field is close to Gaussian. Under such condition, only the k_{\parallel} and k_{\parallel}^2 terms exist in Eq. 23. This results in a Gaussian pairwise velocity PDF, and corresponds to the Gaussian streaming model of correlation function. Numerical evaluation later indeed shows that the expansion of Eq. 23 indeed converges faster than that of Eq. 15. Nevertheless, we find $k_{\parallel}^{3,4}$ terms are non-negligible at $k \gtrsim 0.2h \text{ Mpc}^{-1}$, implying further improvement over the Gaussian streaming approximation.

2.5 Peculiar velocity decomposition

As mentioned above, moment generating function determines the pairwise velocity PDF, and vice versa. There are lots of models based on the pairwise velocity PDF assuming some specific forms of pairwise velocity PDF, such as Gaussian distribution (Reid & White 2011), exponential distribution (Sheth 1996) and so on. Here we investigate the influence of both Gaussian and exponential approximations towards generating function. For brevity, here we only provide one point statistics of velocity PDF, instead of the more complicated two point statistics of pairwise velocity PDF. The statistics from simulation prefer a

mixture of Gaussian and exponential pairwise velocity PDF. At sufficiently large scale with low speed, it is close to Gaussian distribution,

$$p_G(v) = \frac{1}{\sqrt{2\pi\sigma_G^2}} \exp(-v^2/2\sigma_G^2), \quad (24)$$

yet at small scale with severe random motions, it turns to exponential distribution,

$$p_E(v) = \frac{1}{\sqrt{2\sigma_E^2}} \exp(-\sqrt{2}|v|/\sigma_E). \quad (25)$$

Here $\sigma_{G,E}$ is the pairwise velocity dispersion for Gaussian/Exponential components, and $\sigma_G^2 + \sigma_E^2 = \sigma^2$. The corresponding Fourier transformations are,

$$\mathcal{G} = \exp(-\sigma_G^2 k^2/2), \mathcal{E} = \frac{1}{\sigma_E^2 k^2/2 + 1}. \quad (26)$$

Assuming the Gaussian part and exponential part are independent with each other, the generating function could be written as,

$$G \approx \mathcal{G}(\sigma_G)\mathcal{E}(\sigma_E) \quad (27)$$

Under these assumptions, the imaginary part of generating function, $\text{Im}(G)$, vanishes. Gaussian/exponential distributions determine the upper/lower limits of $\text{Re}(G)$.

Furthermore, [Zhang et al. \(2013\)](#) provide a method to decompose the peculiar velocity field into three parts, \mathbf{v}_δ , \mathbf{v}_B , and \mathbf{v}_S . \mathbf{v}_δ is the over-density field correlated part. It dominates at the linear scale where $k \ll k_{NL}$ (NL is short for ‘‘non-linear’’ scale), then vanishes due to the nonlinear evolution at small scale. Differ from \mathbf{v}_δ , the stochastic component \mathbf{v}_S and rotational component \mathbf{v}_B only reveal and dominant at the nonlinear scale. [Zheng et al. \(2013\)](#) verified these theories in N-body simulation. In this paper, we decompose the peculiar velocity into only density correlated (the deterministic) part, and the rest stochastic part ($\mathbf{v}_S + \mathbf{v}_B$ in [Zhang et al. \(2013\)](#)). We denoted them with superscripts L and S respectively, $\mathbf{v}(\mathbf{x}) = \mathbf{v}^L(\mathbf{x}) + \mathbf{v}^S(\mathbf{x})$. In Fourier space,

$$\mathbf{v}^L(\mathbf{k}) = -i \frac{H(z)\delta(\mathbf{k})W(k)}{k^2} \mathbf{k}. \quad (28)$$

Here, the window function,

$$W(k) = \frac{P_{\delta\theta}(k)}{P_{\delta\delta}(k)}. \quad (29)$$

in which, $\theta = -\nabla \cdot \mathbf{v}$ is the divergence of the peculiar velocity. Then the generating function can be expressed in,

$$\begin{aligned} G &= \frac{\langle (1 + \delta_1)(1 + \delta_2) \exp(ik_{\parallel}v) \rangle}{1 + \xi(r)} \\ &= \frac{\langle (1 + \delta_1)(1 + \delta_2) \exp(ik_{\parallel}v^L) \exp(ik_{\parallel}v^S) \rangle}{1 + \xi(r)} \end{aligned} \quad (30)$$

If the density field is log-normal, assume L and S components are independent with each other, we have

$$\ln G = \ln G^L + \ln G^S. \quad (31)$$

G^L is expected to be approximately Gaussian, and the stochastic part G^S should be close to exponential. We can evaluate the convergence of both Eq.(27) and Eq.(31) in simulation.

Table 1: Three sets of halo mass bins for J6610. The mass unit is in $10^{12}M_{\odot}/h$. $\langle M \rangle$ is the mean halo mass. N_h is the total halo number in corresponding halo mass bin.

Set ID	Mass Range	$\langle M \rangle$	$N_h/10^4$
A1($z = 0.0$)	> 10	37.70	8.66
$z = 0.5$	> 10	30.03	6.70
$z = 1.0$	> 10	23.77	4.30
$z = 1.5$	> 10	20.39	2.53
A2($z = 0.0$)	1-10	2.67	69.23
$z = 0.5$	1-10	2.61	66.88
$z = 1.0$	1-10	2.51	59.86
$z = 1.5$	1-10	2.41	50.49
A3($z = 0.0$)	0.1-1	0.27	506.14
$z = 0.5$	0.1-1	0.27	523.57
$z = 1.0$	0.1-1	0.26	527.22
$z = 1.5$	0.1-1	0.26	508.97

3 SIMULATION

We numerically evaluate the generating function G at various k_{\parallel} and $(r_{\parallel}, r_{\perp})$, and the two expansion series (Eq. 15 & 23), in a subset of the CosmicGrowth simulations (Jing 2019). The three simulations are run with a particle-particle-particle-mesh (P³M) code (Jing et al. 2007), boxsize $L_{\text{box}} = 600\text{Mpc } h^{-1}$, and particle number $N_P = 3072^3$. They adopt the identical Λ CDM cosmology, with $\Omega_b = 0.0445$, $\Omega_c = 0.2235$, $\Omega_{\Lambda} = 0.732$, $h = 0.71$, $n_s = 0.968$ and $\sigma_8 = 0.83$. It has three realizations, denoted as J6610, J6611 and J6612 here. The halo catalogs are first identified by a Friends-of-Friends (FoF) algorithm, with the linking length $b = 0.2$ times the mean inter-particle separation. Then all unbound particles have been removed from the catalogs. We select three different halo mass bins, labeled as A1, A2 and A3, at four redshift snapshots, $z \simeq 0, 0.5, 1.0, 1.5$. The mass range, mean mass, and total number of each halo set for J6610 are listed in Table 1. Specifications of J6611 and J6612 are similar.

We use the NGP method with 600^3 grid points to construct the needed fields. The grid size is $L_{\text{grid}} = 1\text{Mpc } h^{-1}$. For each grid, we measure $\alpha_i = \sum_{\gamma} \cos(k_{\parallel} v_{\parallel, \gamma})$, $\beta_i = \sum_{\gamma} \sin(k_{\parallel} v_{\parallel, \gamma})$ and $p_i^n = \sum_{\gamma} v_{\parallel, \gamma}^n$, $n = 0, 1, 2, 3, \dots$. Notice that $p_i^0 = \sum_{\gamma} 1 = (1 + \delta_i)$. The summation \sum_{γ} is over all particles nearest to the i th grid point. The real and imaginary part of the generating function are evaluated separately by the following relation

$$G(k_{\parallel}, \mathbf{r}) = \frac{\langle \beta_1 \beta_2 + \alpha_1 \alpha_2 \rangle_{\mathbf{r}}}{\langle p_1^0 p_2^0 \rangle_{\mathbf{r}}} + i \frac{\langle \alpha_1 \beta_2 - \beta_1 \alpha_2 \rangle_{\mathbf{r}}}{\langle p_1^0 p_2^0 \rangle_{\mathbf{r}}}. \quad (32)$$

The pairwise velocity moments is given by

$$\langle v_{12}^m \rangle = \frac{\langle \sum_{n=0}^m C_m^{m-n} (-1)^n p_1^n p_2^{m-n} \rangle_{\mathbf{r}}}{\langle p_1^0 p_2^0 \rangle_{\mathbf{r}}}. \quad (33)$$

One thing to notice is that, the r.h.s. of Eq. 32 & 33 means that we can utilize FFT to speed up the computation. For each k_{\parallel} , 8 FFTs are needed to evaluate G of all \mathbf{r} pairs, and ≥ 3 FFTs for $\langle v_{12}^m \rangle$. Nevertheless, since we only investigate a dozen \mathbf{r} specifications, we instead measure the above quantities by directly counting the pairs with fixed separation r_{\parallel} and r_{\perp} values. We can choose the Cartesian x , y , z axes of the simulation box as the line of sight, so for each simulation we have 3 independent measurements. With 3 independent simulation realizations, we have 9 independent measurements and we can then estimate the errorbars of the measured properties.

In order to obtain the deterministic and stochastic components of halo peculiar velocity field, first we measure $\mathbf{v}^L(\mathbf{k})$ from Eq. 28. When obtaining the quantities in Eq. 28, 512^3 number of grid points are adopted to construct the necessary fields. Then we do inverse FFT to obtain \mathbf{v}^L in configuration space. Chen et al. (2018) has verified that the large scale velocity bias between halo and dark matter is unity in N-body simulation, and Zhang (2018) provides the possible explanation. Thus here we can treat the

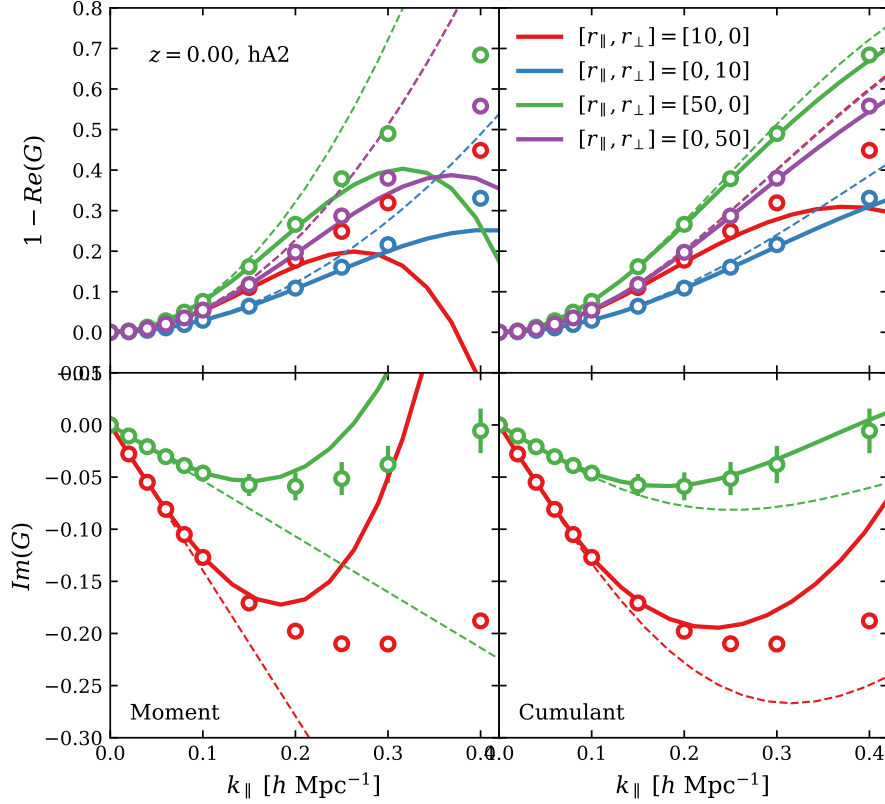


Fig. 1: The pairwise velocity generating function G at $z = 0$, for the halo set A2 ($10^{12}M_{\odot}/h < M < 10^{13}M_{\odot}/h$). Data points (with errorbars) are directly measured from the 3 simulation realizations and the errorbars are r.m.s of the 9 independent measurements (3 simulation realization \times three directions). Top/bottom panels correspond to the real/imaginary part of G respectively. Left/right panels correspond to the results of moment/cumulant expansions. The dash lines cut off at the leading order terms ($\langle v_{12}^{1,2} \rangle, \langle v_{12}^{1,2} \rangle_c$), while the solid lines include the next-to-leading order terms ($\langle v_{12}^{1,2,3,4} \rangle, \langle v_{12}^{1,2,3,4} \rangle_c$). The major finding is that the cumulant expansion works significantly better than the moment expansion. The leading order approximation is excellent at $k \leq 0.1h \text{ Mpc}^{-1}$. Including $\langle v_{12}^{3,4} \rangle$, the cumulant expansion is excellent at $k < 0.2h \text{ Mpc}^{-1}$ for all $(r_{\parallel}, r_{\perp})$ configurations. Furthermore, for $r_{\parallel} \geq 20h \text{ Mpc}^{-1}$, it is excellent to $k \sim 0.4h \text{ Mpc}^{-1}$. Bottom panels ($\text{Im}G$) does not show the configurations with $r_{\parallel} = 0$, for which $\text{Im}G=0$ due to the $v_{\parallel} \leftrightarrow v_{\parallel}$ symmetry.

deterministic velocity component of halos as the underlying dark matter's, $\mathbf{v}_h^L = \mathbf{v}^L$. Finally, we obtain the stochastic component by $\mathbf{v}_h^S = \mathbf{v}_h - \mathbf{v}^L$.

4 NUMERICAL RESULTS AND IMPLICATIONS

The generating function $G \equiv G(k_{\parallel}, r_{\parallel}, r_{\perp})$ depends on k_{\parallel} , r_{\parallel} , r_{\perp} as well as redshift and halo mass. We are not able to show the results of all possible combinations. Instead, we will mainly show the result of mass bin A2. To the same order of moment/cumulant expansion, the accuracy is slightly better for A1, which is less affected by small scale nonlinearities due to larger smoothing associated with the halo mass/size. But since A1 has at least a factor of 10 smaller halo numbers, the measurements are more noiser. In contrast, the accuracy for A3 is slightly worse than A2, while the measurement noise is smaller. Therefore in the main text we only show A2 as the intermediate case. For the redshifts, we mainly show

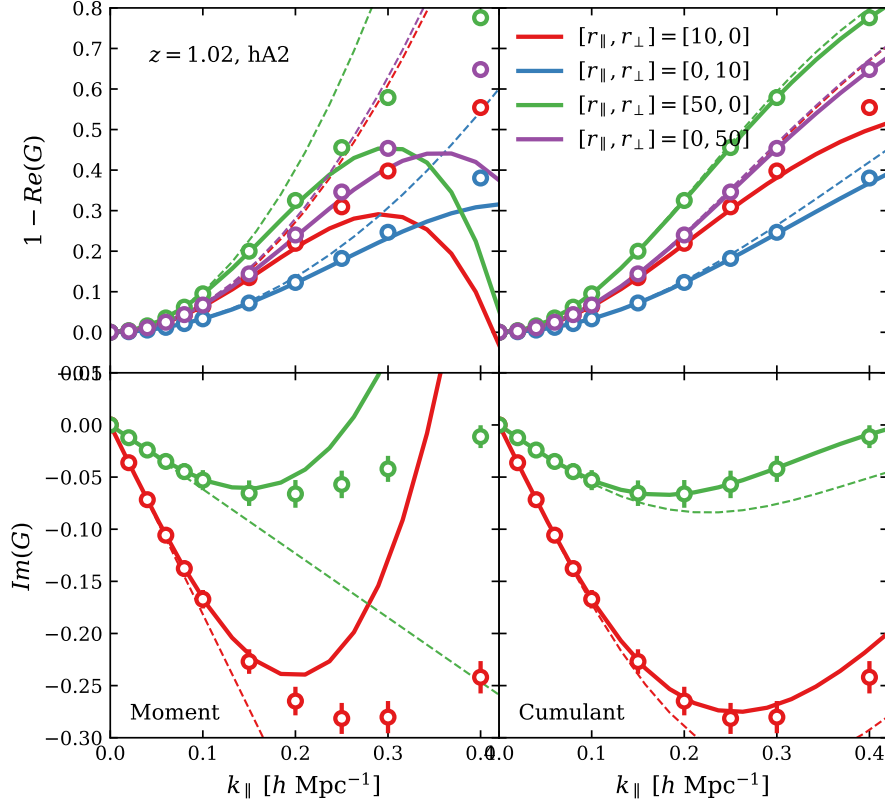


Fig. 2: Similar to Fig. 1 but for redshift $z \approx 1$.

the case of $z = 0$ and when necessary, the case of $z = 1$. For the wavenumber k , the primary target is $k = 0.2h \text{ Mpc}^{-1}$, matching the capability of stage IV projects. But since stage V projects have the capability to reach $k \sim 0.5h \text{ Mpc}^{-1}$, we will also show the results of $k > 0.2h \text{ Mpc}^{-1}$ in the main text.

4.1 $\langle v_{12}^{3,4} \rangle$ terms must be included

Fig. 1 shows G as a function of k_{\parallel} , at $z = 0$ and for $(r_{\parallel}, r_{\perp}) = (10, 0), (0, 10), (50, 0), \&(0, 50)$ (unit in $\text{Mpc } h^{-1}$). We compare the leading order expansion to the simulated G . As a reminder, the leading order moment expansion is $G \simeq 1 + i\langle v_{12} \rangle k_{\parallel} - \langle v_{12}^2 \rangle k_{\parallel}^2 / 2$. The leading order cumulant expansion is $G \simeq \exp(1 + i\langle v_{12} \rangle k_{\parallel} - \langle v_{12}^2 \rangle_c k_{\parallel}^2 / 2)$. All the coefficients ($\langle v_{12}^n \rangle$ and $\langle v_{12}^n \rangle_c$) are measured from the same simulation. The moment expansion becomes inaccurate at $k_{\parallel} = 0.1h \text{ Mpc}^{-1}$, especially for the imaginary part of G . The cumulant expansion remains accurate at $k_{\parallel} = 0.1h \text{ Mpc}^{-1}$. Since the cumulant expansion up to leading order is equivalent to a Gaussian $p(v_{12}|r_{\parallel}, r_{\perp})$, this explains the validity of Gaussian streaming model (Reid & White 2011) at sufficiently large scale. However, at $k_{\parallel} \sim 0.2h \text{ Mpc}^{-1}$, the leading order approximation results into significant error in the imaginary part of G .

Therefore to improve the approximation accuracy at the target $k_{\parallel} = 0.2h \text{ Mpc}^{-1}$, we must include the next-to-leading order terms in the expansion. Then the moment expansion becomes $G \simeq 1 + i[\langle v_{12} \rangle k_{\parallel} - \langle v_{12}^3 \rangle k_{\parallel}^3 / 6] - [\langle v_{12}^2 \rangle_c k_{\parallel}^2 / 2 - \langle v_{12}^4 \rangle k_{\parallel}^4 / 24]$. Nonetheless, the moment expansion still fails at $k_{\parallel} \sim 0.2h \text{ Mpc}^{-1}$, especially for the imaginary part.

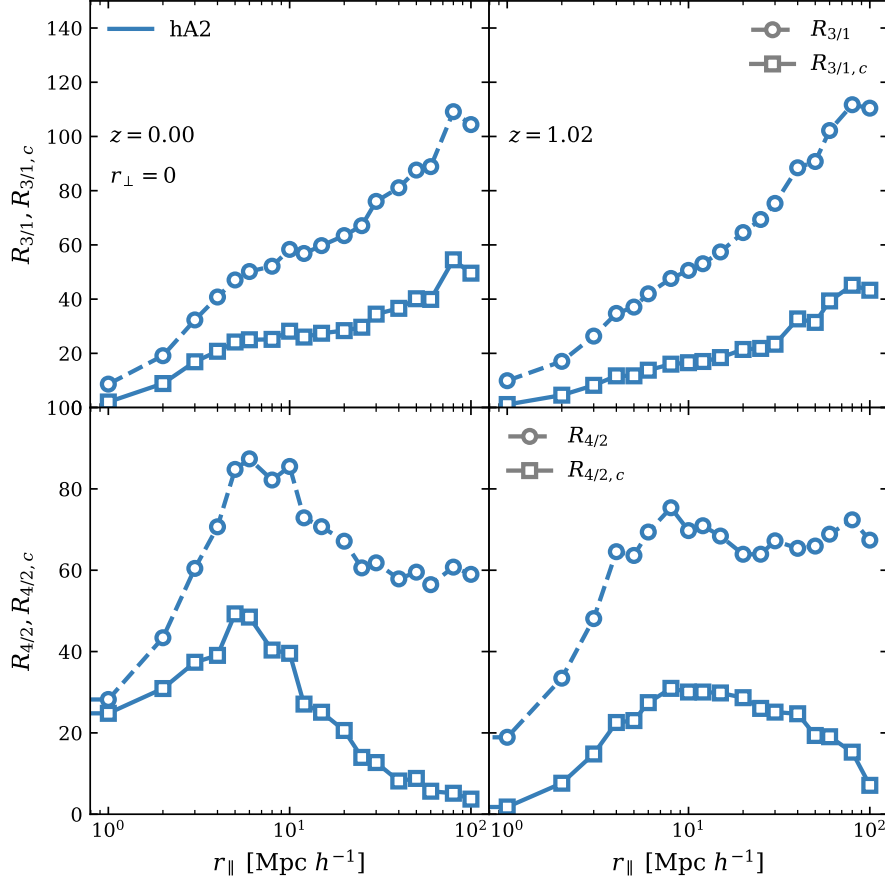


Fig. 3: $R_{3/1} \equiv \langle v_{12}^3 \rangle / \langle v_{12} \rangle$ and $R_{4/2} \equiv \langle v_{12}^4 \rangle / \langle v_{12}^2 \rangle$. These two determine the relative importance of the next-to-leading order terms in the moment expansion. For the cumulant expansion, the corresponding quantities are $R_{3/1,c}$ and $R_{4/2,c}$ respectively. These results explain the necessity of including the next-to-leading terms in the generation function (and RSD). They also explain why the cumulant expansion is better than the moment expansion.

Including the next-to-leading order terms, the cumulant expansion becomes $G \simeq \exp(i[\langle v_{12} \rangle k_{\parallel} - \langle v_{12}^3 \rangle_c k_{\parallel}^3 / 6] - [\langle v_{12}^2 \rangle_c k_{\parallel}^2 / 2 - \langle v_{12}^4 \rangle_c k_{\parallel}^4 / 24])$. This expansion is accurate at $k_{\parallel} = 0.2h \text{ Mpc}^{-1}$. It remains accurate even until $k_{\parallel} \sim 0.4h \text{ Mpc}^{-1}$, unless $r_{\perp} \rightarrow 0$.

The situation is similar at other redshifts (e.g. $z = 1$, Fig. 2). Therefore the first major result of this paper is that, to accurately describe G at $k_{\parallel} \sim 0.2h \text{ Mpc}^{-1}$, we have to include not only $\langle v_{12}^{1,2} \rangle$, but also $\langle v_{12}^{3,4} \rangle$ into the model. Since G completely determines RSD, this also implies that we must include $\langle v_{12}^{3,4} \rangle$ into the modeling of RSD. This will be challenging, since $\langle v_{12}^{3,4} \rangle$ themselves involve LSS correlations up to 6-th order ($\delta^2 v^4$).

We further check the origin of the above finding. The ratio of the k_{\parallel}^3 term to k_{\parallel} term is $R_{3/1} k_{\parallel}^2 / 6$ for the moment expansion, and $R_{3/1,c} k_{\parallel}^2 / 6$ for the cumulant expansion. Here, $R_{3/1} \equiv \langle v_{12}^3 \rangle / \langle v_{12} \rangle$ and $R_{3/1,c} \equiv \langle v_{12}^3 \rangle_c / \langle v_{12} \rangle$. Fig. 3 shows $R_{3/1}$ and $R_{3/1,c}$ for the case of $r_{\perp} = 0$, which is among the most difficult to model for the generating function and RSD. $R_{3/1}$ and $R_{3/1,c}$ have typical values ~ 10 - $100(\text{Mpc } h^{-1})^2$. Therefore for $k_{\parallel} \gtrsim 0.1h \text{ Mpc}^{-1}$, the k_{\parallel}^3 term will become non-negligible comparing

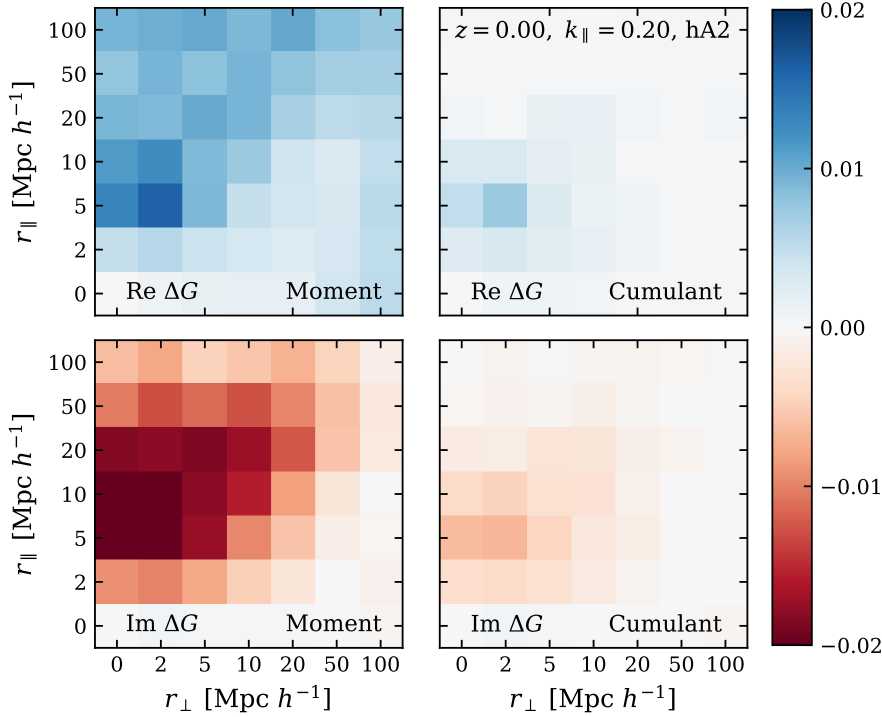


Fig. 4: Accuracies of the moment expansion (left panels) and cumulant expansion (right panels) of the pairwise velocity generating function G at $k_{\parallel} = 0.2h \text{ Mpc}^{-1}$. Both expansions keep the next-to-leading order terms, namely include all $k_{\parallel}^{1,2,3,4}$ terms. Top (bottom) panels are the results of real(imaginary) part of G . This comparison clearly shows that the cumulant expansion works significantly better than the moment expansion. It achieves $|\Delta G| < 0.01$ for all configurations of r_{\perp}, r_{\parallel} . For brevity, we only show the comparison for the halo mass bin A2 at $z = 0$. Results of other mass bins and redshifts are similar.

to the k_{\parallel} term. This problem does not alleviate toward large separation, as we expect. In contrast, $R_{3/1}$ increases and the problem becomes worse at large pair separation. In fact, at $r_{\parallel} \sim 100 \text{ Mpc } h^{-1}$, the moment expansion to third order even fails to correctly predict the sign of $\text{Im}G$ for $k \geq 0.25h \text{ Mpc}^{-1}$.

The ratio of the k_{\parallel}^4 term to k_{\parallel}^2 term is $R_{4/2}k_{\parallel}^2/12$ for the moment expansion, and $R_{4/2,c}k_{\parallel}^2/12$ for the cumulant expansion. Here, $R_{4/2} \equiv \langle v_{12}^4 \rangle / \langle v_{12}^2 \rangle$ and $R_{4/2,c} \equiv \langle v_{12}^4 \rangle_c / \langle v_{12}^2 \rangle$. The numerical results are also shown in Fig. 3. The worst inaccuracy of expanding to 4-th order occurs where $R_{4/2}$ ($R_{4/2,c}$) is largest. This happens at $r_{\parallel} \sim 5 \text{ Mpc } h^{-1}$ and the typical value is $\sim 50(\text{Mpc } h^{-1})^2$. Notice that $\max R_{4/2} < \max R_{3/1}$. Together with the extra factor $1/2$ in the Taylor expansion, the relative correction is significantly smaller in the real part of G than that in the imaginary part.

4.2 Cumulant expansion is better

Fig. 4 shows the errors by neglecting $k_{\parallel}^{n>4}$ terms in the moment/cumulant expansion, in the r_{\perp} - r_{\parallel} plane, for $k_{\parallel} = 0.2h \text{ Mpc}^{-1}$. For the whole range of interest ($r_{\perp} < 100 \text{ Mpc } h^{-1}$, $r_{\parallel} < 100 \text{ Mpc } h^{-1}$), the cumulant expansion is better than the moment expansion. The errors are largest at $r_{\perp} \lesssim 5 \text{ Mpc } h^{-1}$ and $r_{\parallel} \sim 5\text{-}10 \text{ Mpc } h^{-1}$. Nonetheless, $|\Delta G| \lesssim 0.01$.

Fig. 5 shows the errors at $k_{\parallel} = 0.3, 0.4h \text{ Mpc}^{-1}$ for the cumulant expansion. The errors increase with k_{\parallel} , as expected. Also as the case of $k_{\parallel} = 0.2h \text{ Mpc}^{-1}$, the largest error occurs at $r_{\perp} \lesssim 5 \text{ Mpc } h^{-1}$

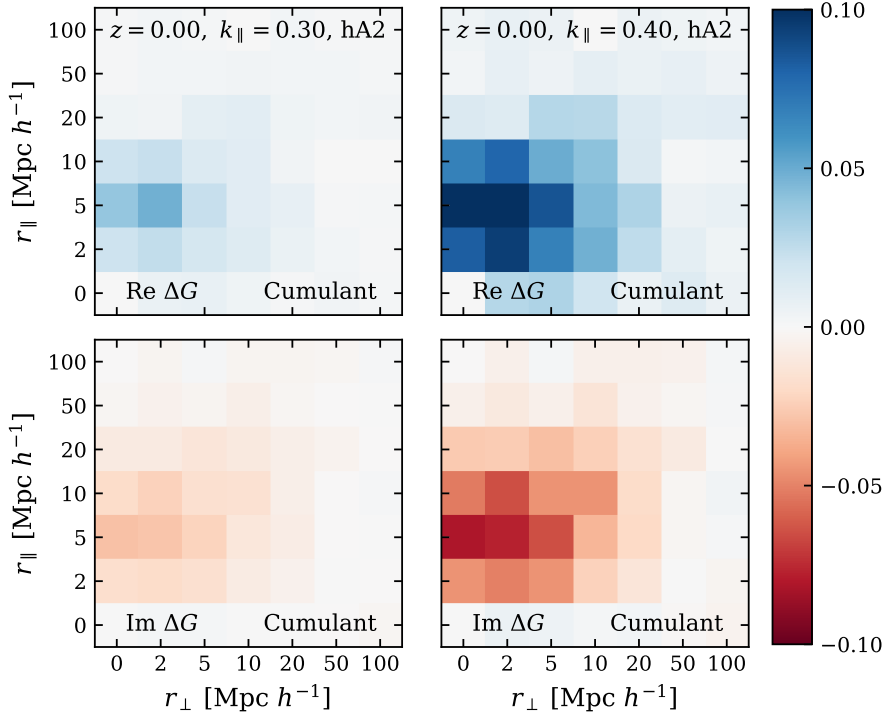


Fig. 5: Similar to Fig. 4, but only for the cumulant expansion at two different $k_z = 0.3$ and 0.4 .

and $r_{\parallel} \sim 5\text{-}10 \text{Mpc } h^{-1}$ and $\max|\Delta G| \sim 0.1$ for $k_{\parallel} = 0.4h \text{Mpc}^{-1}$. Nonetheless, if we only use the region at $r_{\perp} = 20 \text{Mpc } h^{-1}$, the error in G is reduced to ~ 0.01 , even for $k = 0.4h \text{Mpc}^{-1}$. Fig. 6 shows the errors at $k_{\parallel} = 0.2h \text{Mpc}^{-1}$, but for halo set A1 and A3. The cumulant expansion is also excellent.

Therefore the major results of this paper are

$$\begin{aligned}
 G &\simeq \exp \left[-\frac{\langle v_{12}^2 \rangle_c k_{\parallel}^2}{2} + i \langle v_{12} \rangle k_{\parallel} \right] \\
 &\quad \text{for all } \mathbf{r}, \text{ but } k \leq 0.1h \text{Mpc}^{-1}, \\
 &\simeq \exp \left[-\frac{\langle v_{12}^2 \rangle_c k_{\parallel}^2}{2} + \frac{\langle v_{12}^4 \rangle_c k_{\parallel}^4}{24} + i \left(\langle v_{12} \rangle k_{\parallel} - \frac{\langle v_{12}^3 \rangle_c k_{\parallel}^3}{6} \right) \right] \\
 &\quad \text{for all } \mathbf{r}, \text{ but } k \leq 0.2h \text{Mpc}^{-1}, \\
 &\quad \text{or for } r_{\perp} > 20h \text{Mpc}^{-1} \text{ \& } k \leq 0.4h \text{Mpc}^{-1}.
 \end{aligned} \tag{34}$$

4.3 Induced errors in the RSD modelling

Analysis above shows that it's necessary to include at least 3rd and 4-th order pairwise velocity moments/cumulants in the modeling of generating function at $k \gtrsim 0.2h \text{Mpc}^{-1}$. Inaccuracies in the generating function modeling will propagate into inaccuracies in the RSD power spectrum $P^s(k_{\parallel}, k_{\perp})$, correlation function $\xi^s(r_{\parallel}, r_{\perp})$ and the hybrid statistics $P^s(k_{\parallel}, r_{\perp})$. For brevity we only investigate its impact on $P^s(k_{\parallel}, r_{\perp})$.

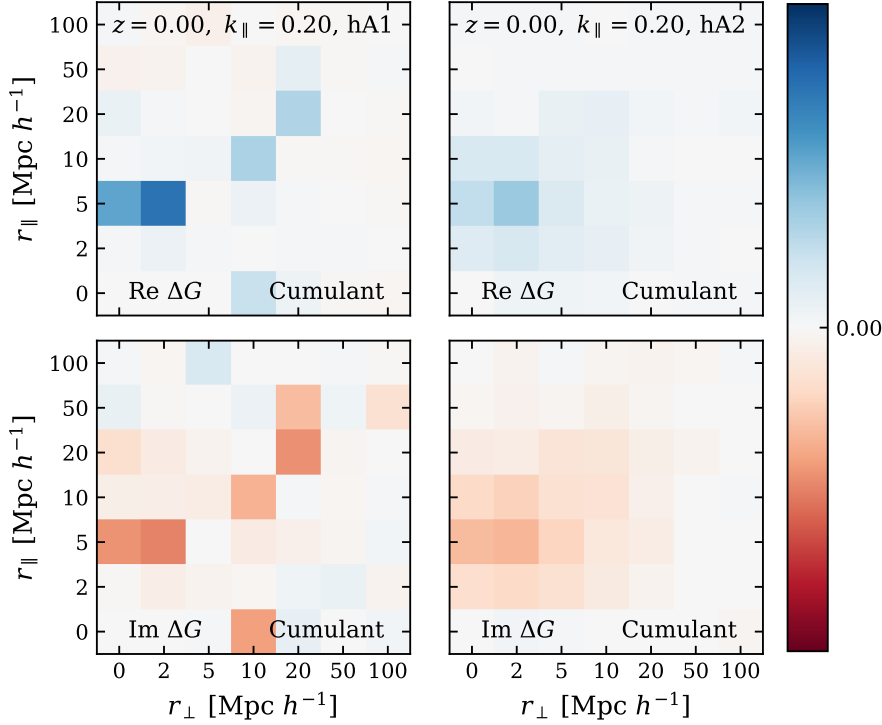


Fig. 6: Similar to Fig. 5, but for the two different halo catalogs A1 and A3 at fixed $k_z = 0.2$.

If the error ΔG has no imaginary part, and is independent of r_{\parallel} , it leads to $\Delta P^s = P^s(k_{\parallel} = 0, r_{\perp})\Delta G = w_p(r_{\perp})\Delta G$. Since the absolute value of ΔG in the cumulant expansion is in general < 0.01 for $k < 0.2h \text{ Mpc}^{-1}$, the resulting error in P^s is $\lesssim 1\%$. But the real situation is more complicated than that, since ΔG is neither real nor independent of r_{\parallel} . For this we have to numerically integrate over Eq. 14 to obtain the resulting error in P^s . This integral involves the oscillating integrand and is numerically challenging to reach better than 1% in P^s , making the accurate quantification of ΔP^s difficult. For this reason, in the current paper we only show the error in the integrand, induced by ΔG .

Since $P^s(k_{\parallel}, r_{\perp})$ is real,

$$P^s(k_{\parallel}, r_{\perp}) = \int Q(k_{\parallel}, r_{\parallel}, r_{\perp}) dr_{\parallel}. \quad (35)$$

Here the integrand

$$Q = [(1 + \xi(r))\text{Re}G(k_{\parallel}, r_{\parallel}, r_{\perp}) - 1] \cos(k_{\parallel}r_{\parallel}) - (1 + \xi(r))\text{Im}G(k_{\parallel}, r_{\parallel}, r_{\perp}) \sin(k_{\parallel}r_{\parallel}). \quad (36)$$

Q in the simulation and the associated error ΔQ by the moment/cumulant expansion to 4-th order are shown in Fig. 7. Since the largest error in G occurs at $r_{\perp} \lesssim 10 \text{ Mpc } h^{-1}$, we only show the cases of $r_{\perp} = 10, 20 \text{ Mpc } h^{-1}$. At $k_{\parallel} = 0.2h \text{ Mpc}^{-1}$, $|\Delta Q| < 0.01$ and for most r_{\parallel} $|\Delta Q| \ll 0.01$, for the cumulant expansion up to the order of $\langle v_{12}^4 \rangle_c$. For comparison, we also show the case of moment expansion, whose error is much larger.

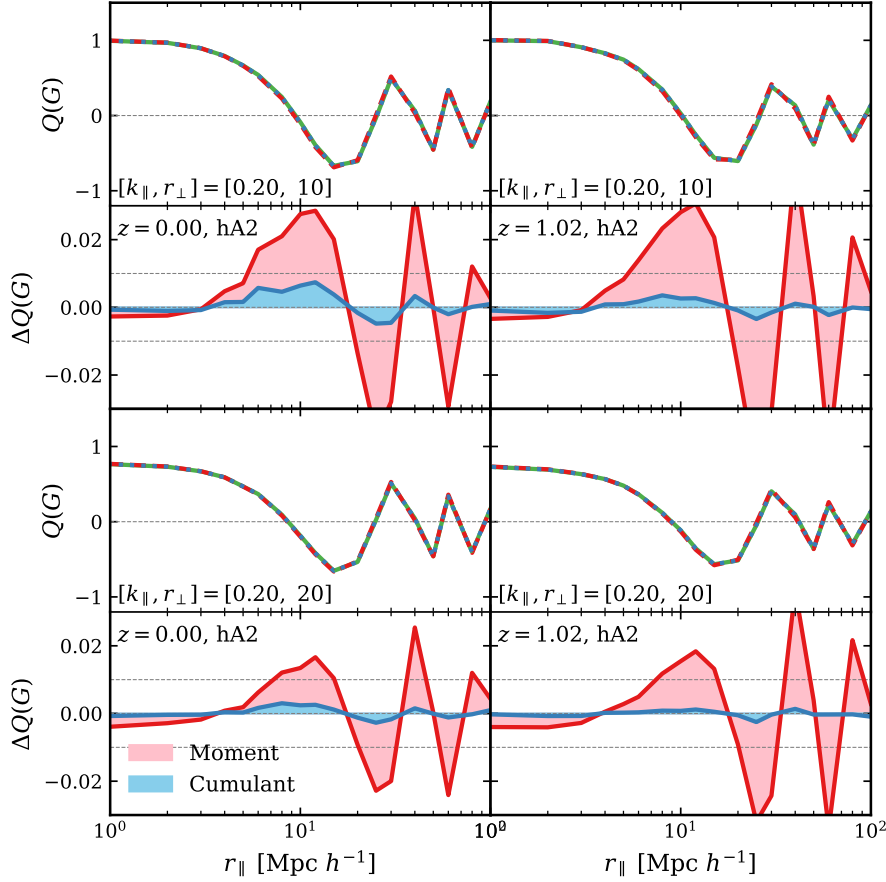


Fig. 7: *upper*: The integral kernel $Q(G)$ for halo set A2 at $z = 0$ (*l.h.s*) and $z = 1$ (*r.h.s*). *lower*: residuals for the two different approaches.

4.4 Peculiar velocity decomposition

Fig. 8 illustrates the results of Eq. 27 for halo sets A1 and A2 at $z = 0$. We first measure the velocity dispersion σ_v . Then consider two extreme cases: Gaussian limit, $\sigma_G = \sigma_v$ and exponential limit, $\sigma_E = \sigma_v$. The upper edge and lower edge of each shaded region correspond to Gaussian and exponential limit respectively. The data points with error bars are direct measurements from halo catalogs. At the non-linear regime (blue and red colored data in Fig. 8), data points are close to the exponential limit. Yet when move to the linear regime, as the green colored data shows, due to the scale is sufficiently large ($r_{||} = 50 \text{Mpc } h^{-1}$) the results are close to the Gaussian limit. The results suggest there is strong possibility that the pairwise velocity PDF is a mixture of Gaussian and exponential distributions. At $k \sim 0.2h \text{Mpc}^{-1}$ scale, it's no longer safe to take the Gaussian distribution assumption. This conclusion matches with above moment/cumulant expansion approaches.

Fig.9 shows the dark matter power spectrum evaluated from N-body simulation for the total velocity field, as well as the two components introduced in Section2.5 at redshift $z = 0$. The behavior of each component is consistent with the descriptions in Section2.5. Fig. 10 is the test for Eq. 31. When G^L and G^S are fully independent, $\ln G^L + \ln G^S$ (solid lines) should be strictly equal to $\ln G$ (dashed lines). The slight deviations implies there's correlation between the deterministic component and stochastic component, especially at the smaller scales (red and blue colored data).

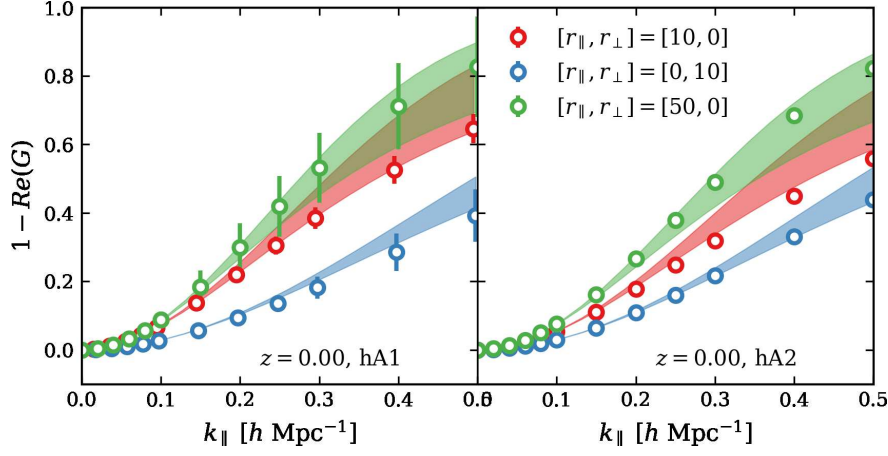


Fig. 8: Test for Eq. 27. The upper edge of the shaded region is Gaussian distribution limit ($\sigma_G^2 = \sigma^2, \sigma_{\mathcal{E}}^2 = 0$), the lower edge is exponential distribution limit ($\sigma_{\mathcal{E}}^2 = \sigma^2, \sigma_G^2 = 0$).

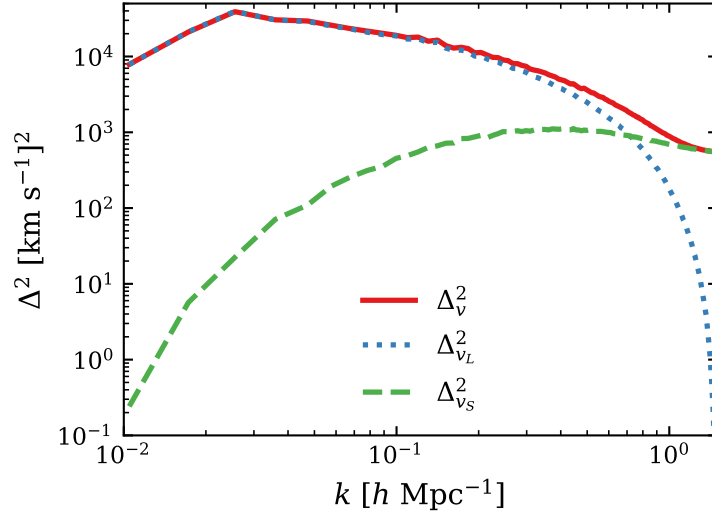


Fig. 9: The dark matter power spectrum for peculiar velocity, deterministic component and stochastic component at $z = 0$. $\Delta^2 = k^3 P(k) / (2\pi^2)$.

Fig. 11 shows the $\ln G^S$ as a function of r_{\parallel} for halo set A3 at $z = 0$ when fix $r_{\perp} = 0$. We demonstrate A3 here because the random motion is more severe for the smaller halos, and therefore the stochastic component should be more significant than A1 and A2. The results suggest the stochastic component is almost scale independent. The real part $\text{Re}(\ln G_S)$ is decided by the $\langle v_{12,S}^m \rangle$, $m = 2, 4, 6, \dots$. Since there is no cross-correlation between two different points 1 and 2 for a stochastic field, the scale dependent part in $\langle v_{12,S}^m \rangle$ vanishes, only the auto-correlation part resides. The non-zero value of $\text{Re}(\ln G_S)$ implies there is Gaussian component in stochastic velocity field. For the imaginary part, as expected, it is not only scale independent but also zero.

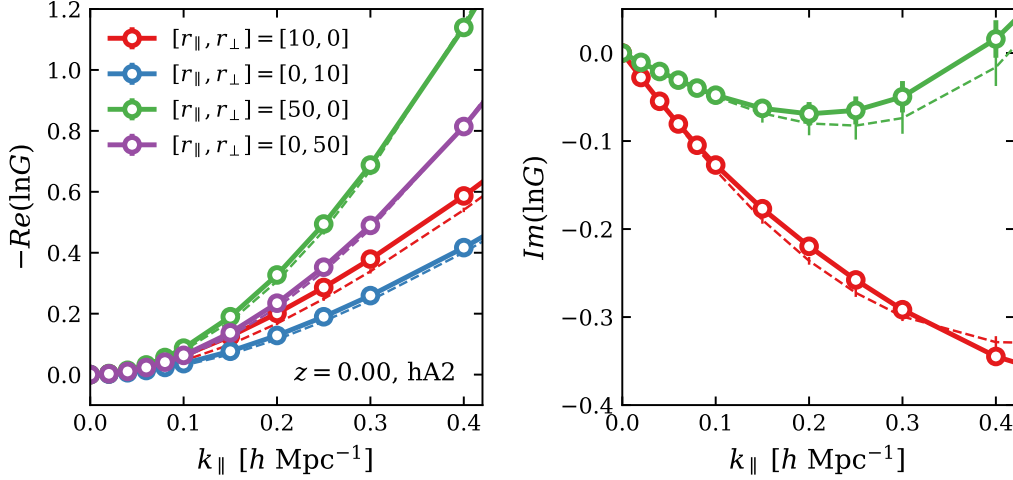


Fig. 10: Test for Eq. 31. Notice the vertical axis here is no longer about G but $\ln G$. The solid lines with data points are $\ln G^L + \ln G^S$, where G^L and G^S is measured from simulation using the velocity decomposition method. The dashed lines are $\ln G$ directly measured from simulation.

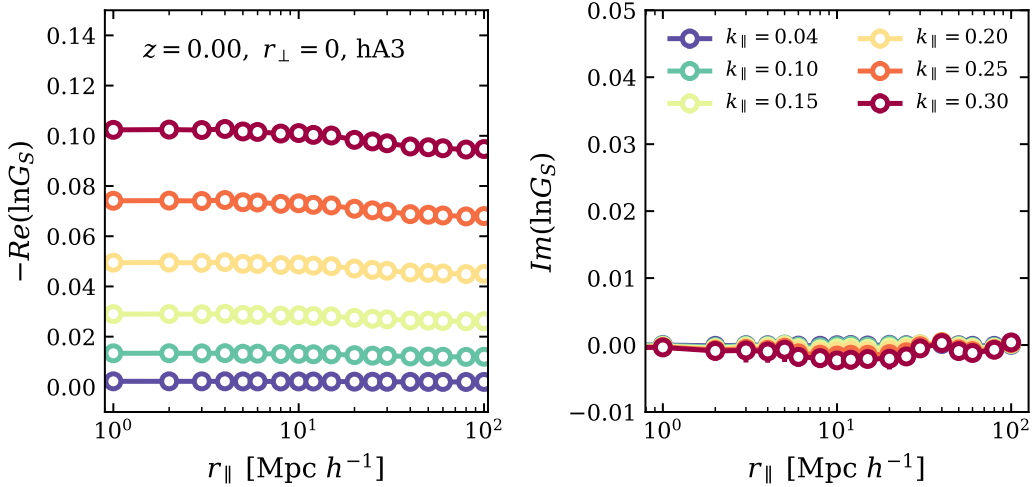


Fig. 11: The moment generating function for stochastic component.

5 CONCLUSIONS AND DISCUSSIONS

In this work, we investigate the convergence of measuring moment generating function in both Moment and Cumulant expansion approaches and find: (1) Cumulant expansion performs much better than the Moment expansion for all halos samples and redshifts investigated. (2) at $k < 0.1h \text{ Mpc}^{-1}$ scale, including only the order of $n = 1, 2$ Cumulants is sufficient for modeling RSD. (3) at $k \sim 0.2h \text{ Mpc}^{-1}$ scale, the order of $n = 1, 2, 3, 4$ Cumulants must be considered. When considering the 3rd and 4th order pairwise velocity moments and cumulants, the cumulant expansion approach performs much better in the Hybrid statistics $P^s(k_{\parallel}, r_{\perp})$.

Studies on the pairwise velocity PDF support a mixture of Gaussian and exponential pairwise velocity PDF. The results also support the above conclusions that the Gaussian streaming model only works at $k < 0.1h \text{ Mpc}^{-1}$. RSD models based on $p(v_{12})$ can not take the Gaussian as well as exponential distribution assumptions at $k \sim 0.2h \text{ Mpc}^{-1}$. Further investigation on the peculiar velocity decomposition suggest a correlation between deterministic and stochastic components at small scale, and a Gaussian mixture part in stochastic component.

Comprehensive further investigations are required to implicate these findings in improving the RSD modeling. In this work, by measuring G , we aim to investigate what is the requirement for the truncation of the peculiar velocity statistics in order to accurately model RSD, and the rationality and reliability to adopt Gaussian or exponential distribution assumptions to the pairwise velocity PDF. Nevertheless, since the full understanding of the pairwise velocity PDF is still a long-standing problem in RSD cosmology, precisely building the association of the expansion coefficients for both moment expansion $\langle v_{12}^n \rangle$, and cumulant expansion $\langle v_{12}^n \rangle_c$, with the cosmological parameters are very difficult. Moreover, in order to apply our method in practice, a complete calculation for the hybrid statistics $P^s(k_{\parallel}, r_{\perp})$ is required. However, in this work, we mainly focus on the moment generating function G , so we just briefly compare the errors of the integrand of Eq.14 for the two different expansions. Eq.14 is an integral for an oscillatory function Q , the FFTLog method (Hamilton 2000) might be adopted when measuring $P^s(k_{\parallel}, r_{\perp})$. We will have more detailed studies on the pairwise velocity PDF and $P^s(k_{\parallel}, r_{\perp})$ in our future works.

Acknowledgements This work was funded by the National Natural Science Foundation of China (NSFC) under No.11621303.

References

- Abdalla, F. B., Bull, P., Camera, S., et al. 2015, in *Advancing Astrophysics with the Square Kilometre Array (AASKA14)*, 17 [2](#)
- Alam, S., Ata, M., Bailey, S., et al. 2017, *MNRAS*, 470, 2617 [2](#)
- Amendola, L., Appleby, S., Avgoustidis, A., et al. 2018, *Living Reviews in Relativity*, 21, 2 [2](#)
- Bautista, J. E., Paviot, R., Magaña, M. V., et al. 2020, arXiv:2007.08993 [2](#)
- Beutler, F., Blake, C., Colless, M., et al. 2012, *MNRAS*, 423, 3430 [1](#)
- Bianchi, D., Chiesa, M., & Guzzo, L. 2015, *MNRAS*, 446, 75 [4](#)
- Bianchi, D., Percival, W. J., & Bel, J. 2016, *MNRAS*, 463, 3783 [4](#)
- Blake, C., Brough, S., Colless, M., et al. 2011, *MNRAS*, 415, 2876 [1](#)
- Chen, J., Zhang, P., Zheng, Y., Yu, Y., & Jing, Y. 2018, *ApJ*, 861, 58 [2, 8](#)
- Chen, S.-F., Vlah, Z., & White, M. 2020, *J. Cosmol. Astropart. Phys.*, 2020, 062 [2](#)
- Chuang, C.-H., Prada, F., Cuesta, A. J., et al. 2013, *MNRAS*, 433, 3559 [1](#)
- Cuesta-Lazaro, C., Li, B., Eggemeier, A., et al. 2020, *MNRAS*, 498, 1175 [4](#)
- de la Torre, S., Guzzo, L., Peacock, J. A., et al. 2013, *A&A*, 557, A54 [1](#)
- DESI Collaboration, Aghamousa, A., Aguilar, J., et al. 2016, arXiv e-prints, arXiv:1611.00036 [2](#)
- Desjacques, V., Jeong, D., & Schmidt, F. 2018a, *Phys. Rep.*, 733, 1 [2](#)
- Desjacques, V., Jeong, D., & Schmidt, F. 2018b, *J. Cosmol. Astropart. Phys.*, 2018, 035 [5](#)
- Fisher, K. B. 1995, *ApJ*, 448, 494 [4](#)
- Guzzo, L., Pierleoni, M., Meneux, B., et al. 2008, *Nature*, 451, 541 [1](#)
- Hamilton, A. J. S. 2000, *MNRAS*, 312, 257 [18](#)
- Hawkins, E., Maddox, S., Cole, S., et al. 2003, *MNRAS*, 346, 78 [1](#)
- Howlett, C., Ross, A. J., Samushia, L., Percival, W. J., & Manera, M. 2015, *MNRAS*, 449, 848 [2](#)
- Huterer, D., & Shafer, D. L. 2018, *Reports on Progress in Physics*, 81, 016901 [2](#)
- Jing, Y. 2019, *Science China Physics, Mechanics, and Astronomy*, 62, 19511 [8](#)
- Jing, Y. P., Suto, Y., & Mo, H. J. 2007, *ApJ*, 657, 664 [8](#)
- Johnson, A., Blake, C., Koda, J., et al. 2014, *MNRAS*, 444, 3926 [1](#)
- Juszkiewicz, R., Fisher, K. B., & Szapudi, I. 1998, *ApJ*, 504, L1 [4](#)

- Kaiser, N. 1987, *MNRAS*, 227, 1 [1](#)
- Kuruvilla, J., & Porciani, C. 2018, *MNRAS*, 479, 2256 [4](#)
- Li, Z., Jing, Y. P., Zhang, P., & Cheng, D. 2016, *ApJ*, 833, 287 [2](#)
- Matsubara, T. 2008, *Phys. Rev. D*, 77, 063530 [3](#)
- Mohammad, F. G., Granett, B. R., Guzzo, L., et al. 2018, *A&A*, 610, A59 [2](#)
- Okumura, T., Seljak, U., & Desjacques, V. 2012a, *J. Cosmol. Astropart. Phys.*, 2012, 014 [2](#), [3](#)
- Okumura, T., Seljak, U., McDonald, P., & Desjacques, V. 2012b, *J. Cosmol. Astropart. Phys.*, 2012, 010 [2](#)
- Okumura, T., Hikage, C., Totani, T., et al. 2016, *PASJ*, 68, 38 [2](#)
- Peacock, J. A., Cole, S., Norberg, P., et al. 2001, *Nature*, 410, 169 [1](#)
- Peebles, P. J. E. 1980, *The large-scale structure of the universe* [1](#), [2](#), [4](#)
- Perlmutter, S., Aldering, G., Goldhaber, G., et al. 1999, *ApJ*, 517, 565 [1](#)
- Pezzotta, A., de la Torre, S., Bel, J., et al. 2017, *A&A*, 604, A33 [1](#)
- Reid, B. A., & White, M. 2011, *MNRAS*, 417, 1913 [4](#), [6](#), [10](#)
- Reid, B. A., Samushia, L., White, M., et al. 2012, *MNRAS*, 426, 2719 [1](#)
- Riess, A. G., Filippenko, A. V., Challis, P., et al. 1998, *AJ*, 116, 1009 [1](#)
- Samushia, L., Percival, W. J., & Raccanelli, A. 2012, *MNRAS*, 420, 2102 [1](#)
- Scoccimarro, R. 2004, *Phys. Rev. D*, 70, 083007 [1](#), [2](#), [3](#), [4](#), [5](#)
- Seljak, U., & McDonald, P. 2011, *J. Cosmol. Astropart. Phys.*, 2011, 039 [2](#), [3](#)
- Sheth, R. K. 1996, *MNRAS*, 279, 1310 [4](#), [6](#)
- Simpson, F., Blake, C., Peacock, J. A., et al. 2016, *Phys. Rev. D*, 93, 023525 [1](#)
- Song, Y.-S., Zheng, Y., Taruya, A., & Oh, M. 2018, *J. Cosmol. Astropart. Phys.*, 2018, 018 [3](#)
- Spergel, D., Gehrels, N., Baltay, C., et al. 2015, *arXiv e-prints*, arXiv:1503.03757 [2](#)
- Tamone, A., Raichoor, A., Zhao, C., et al. 2020, *arXiv:2007.09009* [2](#)
- Taruya, A., Nishimichi, T., & Saito, S. 2010, *Phys. Rev. D*, 82, 063522 [3](#), [5](#)
- Tegmark, M., Eisenstein, D. J., Strauss, M. A., et al. 2006, *Phys. Rev. D*, 74, 123507 [1](#)
- Tinker, J. L. 2007, *MNRAS*, 374, 477 [4](#)
- Tojeiro, R., Percival, W. J., Brinkmann, J., et al. 2012, *MNRAS*, 424, 2339 [1](#)
- Vlah, Z., & White, M. 2019, *J. Cosmol. Astropart. Phys.*, 2019, 007 [2](#)
- White, M., Reid, B., Chuang, C.-H., et al. 2015, *MNRAS*, 447, 234 [2](#)
- Zhang, P. 2018, *ApJ*, 869, 74 [2](#), [8](#)
- Zhang, P., Pan, J., & Zheng, Y. 2013, *Phys. Rev. D*, 87, 063526 [2](#), [3](#), [4](#), [7](#)
- Zhao, J., & Chen, J. 2021, *RAA*, 21, 28 [2](#)
- Zheng, Y., & Song, Y.-S. 2016, *J. Cosmol. Astropart. Phys.*, 2016, 050 [3](#)
- Zheng, Y., Song, Y.-S., & Oh, M. 2019, *J. Cosmol. Astropart. Phys.*, 2019, 013 [3](#)
- Zheng, Y., Zhang, P., Jing, Y., Lin, W., & Pan, J. 2013, *Phys. Rev. D*, 88, 103510 [3](#), [4](#), [7](#)